A&A 528, A69 (2011)
DOI: 10.1051/0004-6361/201016417

Astronomy & Astrophysics

R-matrix electron-impact excitation data for the Li-like iso-electronic sequence including Auger and radiation damping⋆

G. Y. Liang and N. R. Badnell

Department of Physics, University of Strathclyde, Glasgow, G4 0NG, UK
e-mail: guiyun.liang@strath.ac.uk

Received 28 December 2010 / Accepted 27 January 2011

ABSTRACT

We present results for the electron-impact excitation of all Li-like ions from Be^{+} to Kr^{33+} which we obtained using the radiation- and Auger-damped intermediate-coupling frame transformation *R*-matrix approach. We have included both valence- and core-electron excitations up to the $1s^2 5l$ and $1s2l4l'$ levels, respectively. A detailed comparison of the target structure and collision data has been made for four specific ions (O^{5+}, Ar^{15+}, Fe^{23+} and Kr^{33+}) spanning the sequence so as to assess the accuracy for the entire sequence. Effective collision strengths (Υs) are presented at temperatures ranging from $2 \times 10^2 (z+1)^2$ K to $2 \times 10^6 (z+1)^2$ K (where z is the residual charge of the ions, i.e. $Z-3$). Detailed comparisons for the Υs are made with the results of previous calculations for several ions which span the sequence. The radiation and Auger damping effects were explored for core-excitations along the iso-electronic sequence. Furthermore, we examined the iso-electronic trends of effective collision strengths as a function of temperature.

Key words. atomic data – atomic processes – plasmas

1. Introduction

Li-like ions are of importance both in astrophysics and in theoretical and experimental atomic physics. Satellite lines arising from transitions of the type $1s2lnl' \rightarrow 1s^2 2l$ (where the generation of $1s2lnl'$ states could be from dielectronic recombination of He-like ions or inner-shell excitation of Li-like ions), were observed in solar flare spectra by the Rentgenowsky Spektrometr s Izognutymi Kristalami (RESIK) instrument on the Russian CORONAS-F mission, launched on 2001 July 31 (Phillips et al. 2006). These satellite lines complicate the analysis of the spectrum around the He-like transition lines but they are important diagnostics of the electron density and temperature of a plasma (Phillips et al. 2006; Nahar et al. 2009; Oelgoetz et al. 2009, and references therein). Atomic data for the dielectronic recombination process populating the $1s2lnl'$ levels has been reported by Bautista & Badnell (2007).

For the case of outer-shell transitions, some $n = 2 \rightarrow 2$ transition lines in Mg^{9+}–Ni^{25+} were recorded in the early solar flare observation by Widing & Purcell (1976). These have been extensively used in a variety of diagnostic applications, for which accurate atomic data are needed.

The group of Sampson carried-out early work to provide comprehensive atomic data for Li-like ions using the non-resonant relativistic distorted-wave (DW) method. Zhang et al. (1990) calculated collision strengths (Ω) for $n = 2 \rightarrow n = 3, 4, 5$ excitations for the 85 ions with nuclear charge number Z: $8 \leq Z \leq 92$. These data are still extensively used by current astrophysical modelling codes, e.g. CHIANTI v6 (Dere et al. 2009). Sampson and co-authors (1985a,b; Zhang et al. 1986; Goett & Sampson 1983) reported the collision strengths of inner-shell ($n \leq 3$) excitations in the Li-like ions with Z: $6 \leq Z \leq 74$. These were obtained using a Coulomb-Born-Exchange (CBE) method. Their data is the main source used by CHIANTI v6 to model the satellite lines of He-like ions.

We turn next to *R*-matrix calculations, which take account of resonances normally omitted by the DW and CBE methods. Berrington & Tully (1997) calculated the valence-electron impact excitation of Fe^{23+} (up to $n = 5$) using the Breit-Pauli *R*-matrix method. Gorczyca & Badnell (1996) demonstrated significant reduction of the resonance contribution due to radiation damping in the K-shell excitation of Fe^{25+} and Mo^{41+}. Subsequently, Ballance et al. (2001) performed a Breit-Pauli *R*-matrix calculation including radiation damping for the inner-shell excitations ($1s^2 nl \rightarrow 1s2ln'l'$, where $n, n' \leq 3$) in Fe^{22+} and Fe^{23+}. Furthermore, taking Auger damping into account, Whiteford et al. (2002) performed new calculations for these (to $n = 3$) inner-shell excitations in Ar^{15+} and Fe^{23+}, using an intermediate-coupling frame transformation (ICFT) *R*-matrix method. A complete excitation dataset for the Ar^{15+} and Fe^{23+} ions was presented in their work by incorporating data from a separate calculation for outer-shell excitations up to levels of the $n = 5$ complex. There appears to be no previous inner-shell electron-impact excitation work using the close-coupling method for all other ions in this iso-electronic sequence.

For valence-electron excitations, Griffin et al. (2000) carried-out LS-coupling *R*-matrix with pseudo-states (RMPS) calculations for C^{3+} and O^{5+}. Similar calculations for Be^{+} ($n \leq 5$) were performed by Ballance et al. (2003). Aggarwal and co-authors (2004a,b, 2010) reported results for $n \leq 5$ for N^{4+}, O^{5+}, F^{6+}, Ne^{7+}, Na^{8+}, Ar^{15+} and Fe^{23+} which were obtained by using the Dirac *R*-matrix method as implemented in DARC.

Here, we report-on calculations for the electron-impact excitation of the Li-like iso-electronic sequence ions from Be^{+} to

⋆ These data are made available in the archives of APAP via http://www.apap-network.org, OPEN-ADAS via http://open.adas.ac.uk, as well as anonymous ftp to cdsarc.u-strasbg.fr (130.79.128.5) or via http://cdsweb.u-strasbg.fr/cgi-bin/qcat?J/A+A/528/A69

Kr^{33+} which were made using the ICFT R-matrix method. The main focus of the present work is on the inner-shell transitions to $n = 4$ which contribute to the population of the upper levels ($1s2lnl'$) of the He-like satellite lines. Separate outer-shell calculations were made which went up to $n = 5$.

This paper is one of our series of works on iso-electronic sequences: F-like, Witthoeft et al. (2007), Ne-like, Liang & Badnell (2010), Na-like, Liang et al. (2009a,b). This work is part of the UK Atomic Processes for Astrophysical Plasmas (APAP) network[1].

The remainder of this paper is organized as follows. In Sect. 2, we discuss details of the calculational method and pay particular attention to comparing our underlying atomic structure results with those of previous workers. The model for scattering calculation is outlined in Sect. 3. The excitation results themselves are discussed in Sect. 4.

2. Sequence calculation

The aim of this work is to perform R-matrix calculations employing the ICFT method (see Griffin et al. 1998) for all Li-like ions from Be^{+} to Kr^{33+}. Our approach to the valence- and core-excitation data is to perform the two calculations independently and later merge the effective collision strengths (Υ) back together into a single dataset for each ion.

The reason for this approach is that the number of R-matrix continuum basis orbitals required increases with box size (which scales as n^2) and also with scattering energy. Inner-shell excitations require a large scattering energy and $n = 5$ gives rise to a large box size. The two together result-in too large an $(N + 1)$-electron Hamiltonian for Auger plus radiation damped R-matrix calculations along an entire sequence. There are also numerical stability issues when the number of continuum basis orbitals exceeds 100 per orbital l.

The close-coupling (CC) and configuration interaction (CI) expansions used consist of the $1s^2\{2,3,4,5\}l$ (14 LS terms, 24 fine-structure levels) and $1s^2\{2,3,4\}l$, $1s2l\{2,3,4\}l'$ (89 LS terms, 195 fine-structure levels) configurations for the valence- and core-excitation calculations, respectively.

2.1. Structure: level energies

The target wavefunctions (1s−5g) were obtained from AUTOSTRUCTURE (AS, Badnell 1986) using the Thomas-Femi-Dirac-Amaldi model potential. Relativistic effects were included perturbatively from the one-body Breit-Pauli operator (viz. mass-velocity, spin-orbit and Darwin) without valence-electron two-body fine-structure operators. This is consistent with the operators included in the standard Breit-Pauli R-matrix suite of codes. The radial scaling parameters, λ_{nl} ($n = 1$−5; $l \in$ s, p, d, and f, were obtained separately for each ion by a two-step optimization procedure. In the first step, the energy of the $1s^22l$ was minimized by varying the λ_{1s}, λ_{2s} and λ_{2p} scaling parameters. Then, the energy of the $1s^2\{3,4,5\}l$ configurations was minimized by varying the $\lambda_{\{3,4,5\}l}$ scaling parameters. In the calculation including doubly-excited configurations, the energy of the $1s^2\{3,4\}l$ configurations was minimized by varying the $\lambda_{\{3,4\}l}$ scaling parameters. In order to maintain consistency and so as not to introduce arbitrary changes along the sequence, the optimization procedure is done automatically in AUTOSTRUCTURE without any manual re-adjustment. The resultant scaling parameters are listed in Table 1. We took λ_{5g} to be unity since it is insensitive to optimization and the atomic structure itself is insensitive to it.

A comparison of level energies is made with the experimentally derived data available from the compilation of NIST v3[2] and with other theoretical results for several specific ions (O^{5+}, Ar^{15+}, Fe^{23+}, and Kr^{33+}) spanning the sequence so as to assess the accuracy of our present structure over the entire iso-electronic sequence – see (the composite) Table 2. The low-lying level energies of all ions agree to within about 1%. The present calculations also show a good agreement (1%) with previous results obtained by using GRASP (Aggarwal et al. 2004a,b, 2010) and the Dirac-Fock-Slater method (Zhang et al. 1990) for O^{5+}, Ar^{15+} and Fe^{23+} [3]. It should be noted that there can be large factor differences in energy separations between closely-spaced levels arising from different configurations, e.g. $5f_j$−$5g_{j'}$ etc. For higher-lying levels, our energies differ from NIST's by at most 0.5% (see Table 2). Checks with AS calculations including both the two-body fine-structure and quantum-electrodynamic (QED) effects revealed the two-body fine-structure contribution to be negligible when compared with those of QED for these Li-like ions. (Two-body fine-structure and QED operators have not yet been incorporated into the present R-matrix codes, but such work is in progress – Eissner, private communication.)

2.2. Structure: line strength S

A further test of our structure calculation is to compare line strengths (S_{ij} for a given $i \leftarrow j$ transition). In terms of the transition energy E_{ji} (Ryd) for the $j \rightarrow i$ transition, the absorption oscillator strength, f_{ij}, can be written as

$$f_{ij} = \frac{E_{ji}}{3g_i} S, \tag{1}$$

and the transition probability or Einstein's A-coefficient, A_{ji}, as

$$A_{ji}(\mathrm{au}) = \frac{1}{2}\alpha^3 \frac{g_i}{g_j} E_{ji}^2 f_{ij}, \tag{2}$$

where α is the fine structure constant, and g_i, g_j are the statistical weight factors of the initial and final states, respectively. Table 3 shows a comparison of line strengths for the most prominent satellite lines (Gabriel 1972) for several ions (O^{5+}, Ar^{15+}, Fe^{23+} and Kr^{33+}) spanning the sequence.

To-date, the Li-like inner-shell line-strength data ($n = 2p \rightarrow 1s$) calculated by Goett & Sampson (1983) is the main source of data used in astrophysical modelling. So, a comparison with their results, and others, has been made to assess the present structure results for S over the iso-electronic sequence – see Table 3. For O^{5+}, results for most (76%) of the listed transitions agree to within 15% . For Ar^{15+}, there is good agreement with Goett & Sampson (1983) – about 86% of transitions are within 15%. The present results also show excellent agreement with the data of Whiteford et al. (2002) also obtained using AUTOSTRUCTURE. For Fe^{23+}, almost all transition lines show excellent agreement (to within 5%) with the results of Whiteford et al. (2002) except for the s-line – there is somewhat of a spread of results for this line. Most of transitions (64%) show agreement to within 15% between the present AS and the multiconfiguration Dirac-Fock (MCDF) calculation of Chen (1972), in which the Breit and QED contributions have been included in

[1] http://www.apap-network.org

[2] http://physics.nist.gov/PhysRefData/ASD/index.html

[3] For conciseness, the GRASP results (McKeown et al. 2004b) for Fe^{23+} are not listed in Table 2 but the comparison is very similar to Ar^{15+}.

Table 1. Thomas-Fermi potential scaling factors used by AUTOSTRUCTURE for the outer-shell calculations (see text for details).

Ion	1s	2s	2p	3s	3p	3d	4s	4p	4d	4f	5s	5p	5d	5f
Be	1.26220	0.95294	0.79908	0.94457	0.79766	0.71121	0.94335	0.79778	0.71267	0.89615	0.94398	0.79888	0.71498	0.69709
B	1.26855	0.97899	0.84268	0.96958	0.83983	0.75956	0.96833	0.83995	0.76070	0.84971	0.96925	0.84156	0.76285	0.73398
C	1.27206	0.99491	0.86843	1.08212	0.86491	0.78754	0.98466	0.86479	0.78918	0.01715	0.98531	0.86651	0.79200	0.76894
N	1.27433	1.00560	0.88541	0.99501	0.88145	0.80706	0.99365	0.88123	0.80795	0.87641	0.99490	0.88244	0.81094	0.78572
O	1.27592	1.01330	0.89766	1.00231	0.89263	0.81962	1.00090	0.89264	0.82155	0.88781	1.00267	0.89410	0.82480	0.79836
F	1.27708	1.01900	0.90652	1.00748	0.90137	0.82978	1.00632	0.90117	0.83202	0.92080	1.00767	0.90270	0.83556	0.81770
Ne	1.27799	1.02346	0.91350	1.01200	0.90786	0.83823	1.00986	0.90769	0.83982	0.82573	1.01195	0.90920	0.84313	0.81985
Na	1.27871	1.02718	0.91907	1.01537	0.91386	0.84411	1.01393	0.91293	0.84623	0.90169	1.01539	0.91441	0.84784	0.83768
Mg	1.27930	1.03013	0.92365	1.01801	0.91745	0.84911	1.01666	0.91720	0.85103	0.97842	1.01805	0.91875	0.85430	0.83558
Al	1.27978	1.03249	0.92744	1.02000	0.92086	0.85314	1.01892	0.92074	0.85522	0.97734	1.02000	0.92235	0.85853	0.83986
Si	1.28020	1.03447	0.93064	1.02229	0.92303	0.85820	1.02083	0.92294	0.86031	0.99336	1.02230	0.92504	0.86440	0.84214
P	1.28056	1.03623	0.93338	1.02393	0.92664	0.85968	1.02267	0.92629	0.86165	0.99434	1.02410	0.92792	0.86559	0.84554
S	1.28087	1.03777	0.93576	1.02526	0.92883	0.86236	1.02391	0.92845	0.86423	1.00598	1.02566	0.93011	0.86814	0.84759
Cl	1.28113	1.03933	0.93783	1.02650	0.93079	0.86475	1.02509	0.93044	0.86662	1.00570	1.02722	0.93204	0.87059	0.84887
Ar	1.28136	1.04052	0.93965	1.02761	0.93258	0.86682	1.02632	0.93219	0.86863	1.01227	1.02802	0.93350	0.87282	0.85031
K	1.28209	1.04102	0.93941	1.02867	0.93409	0.86891	1.02731	0.93362	0.87074	1.01121	1.02854	0.93522	0.87476	0.85148
Ca	1.28175	1.04229	0.94272	1.02971	0.93534	0.87068	1.02841	0.93499	0.87320	1.00370	1.02992	0.93664	0.87654	0.85276
Sc	1.28193	1.04314	0.94401	1.03128	0.93667	0.87263	1.02921	0.93620	0.87438	0.98597	1.03061	0.93744	0.87959	0.87433
Ti	1.28209	1.04415	0.94336	1.03207	0.93777	0.87405	1.02994	0.93730	0.87576	1.00842	1.03134	0.93854	0.88442	0.87359
V	1.28224	1.04485	0.94626	1.03172	0.93876	0.87527	1.03036	0.93824	0.87687	1.03745	1.03264	0.93998	0.88083	0.85574
Cr	1.28236	1.04549	0.94745	1.03251	0.93970	0.87677	1.03066	0.93913	0.87820	1.03462	1.03234	0.94087	0.88204	0.85563
Mn	1.28249	1.04607	0.94835	1.03266	0.94163	0.87711	1.03161	0.94008	0.87911	1.05064	1.03319	0.94174	0.88301	0.85701
Fe	1.28261	1.04660	0.94896	1.03313	0.94135	0.87877	1.03167	0.94084	0.88032	1.04433	1.03370	0.94207	0.88450	0.85595
Co	1.28280	1.04686	0.94994	1.03358	0.94108	0.88330	1.03211	0.94079	0.88490	1.05000	1.03418	0.94279	0.88848	0.86861
Ni	1.28287	1.04757	0.95474	1.03399	0.94174	0.88392	1.03252	0.94144	0.88552	1.04000	1.03462	0.94344	0.88910	0.86709
Cu	1.28290	1.04799	0.95136	1.03437	0.94238	0.88449	1.03290	0.94206	0.88609	1.04301	1.03505	0.94406	0.88967	0.86587
Zn	1.28301	1.04839	0.95206	1.03473	0.94290	0.88518	1.03326	0.94263	0.88661	1.05384	1.03535	0.94453	0.89020	0.86629
Ga	1.28307	1.04876	0.95272	1.03575	0.94442	0.88375	1.03414	0.94376	0.88447	0.89380	1.03580	0.94549	0.88803	0.85918
Ge	1.28313	1.04911	0.95269	1.03535	0.94399	0.88597	1.03389	0.94367	0.88758	1.06038	1.03614	0.94566	0.89117	0.86168
As	1.28319	1.04943	0.95317	1.03572	0.94543	0.88445	1.03472	0.94482	0.88609	1.07506	1.03646	0.93754	0.88944	0.86013
Se	1.28326	1.04975	0.95371	1.03602	0.94485	0.88782	1.03521	0.94452	0.88938	1.04314	1.03689	0.94650	0.89285	0.89000
Br	1.28329	1.05004	0.95416	1.03628	0.94728	0.87994	1.03591	0.94648	0.88231	1.06575	1.03719	0.94691	0.88770	0.83535
Kr	1.28335	1.05031	0.95457	1.03666	0.94579	0.88873	1.03501	0.94542	0.88980	1.05986	1.03749	0.94738	0.89367	0.88985

Table 1. continued.

Ion	1s	2s	2p	3s	3p	3d	4s	4p	4d	4f
Be	1.26184	0.95482	0.80563	0.94614	0.79939	0.71712	0.94575	0.80031	0.72253	0.89290
B	1.26941	0.98145	0.84871	0.97191	0.84175	0.76433	0.97153	0.84272	0.76957	0.89579
C	1.27403	0.99759	0.87379	0.98723	0.86670	0.79331	0.98706	0.86760	0.79895	0.86160
N	1.27685	1.00828	0.89033	0.99779	0.88302	0.81162	0.99694	0.88415	0.81755	0.89765
O	1.27895	1.01594	0.90207	1.00463	0.89456	0.82496	1.00474	0.89563	0.83075	0.99000
F	1.28049	1.02155	0.91054	1.01036	0.90308	0.83523	1.01000	0.90410	0.84055	0.99000
Ne	1.28169	1.02607	0.91728	1.01437	0.90966	0.84264	1.01437	0.91067	0.84821	0.99000
Na	1.28265	1.02943	0.92257	1.01811	0.91491	0.84839	1.01778	0.91587	0.85351	0.99000
Mg	1.28343	1.03229	0.92693	1.02068	0.91919	0.85310	1.02002	0.92012	0.85826	0.99000
Al	1.28409	1.03471	0.93056	1.02338	0.92275	0.85706	1.02271	0.92366	0.86230	0.99000
Si	1.28463	1.03666	0.93361	1.02470	0.92509	0.86246	1.02459	0.92640	0.86792	0.99341
P	1.28510	1.03837	0.93622	1.02631	0.92840	0.86341	1.02619	0.92890	0.86877	0.99694
S	1.28554	1.03966	0.93847	1.02802	0.93062	0.86620	1.02783	0.93142	0.87127	0.99405
Cl	1.28586	1.04139	0.94045	1.02886	0.93172	0.87059	1.02877	0.93299	0.87546	0.99869
Ar	1.28617	1.04253	0.94219	1.03003	0.93419	0.87071	1.03023	0.93503	0.87574	0.98643
K	1.28646	1.04355	0.94373	1.03184	0.93630	0.87193	1.03128	0.93659	0.87698	1.00466
Ca	1.28665	1.04420	0.94510	1.03169	0.93636	0.87971	1.03160	0.93751	0.88395	0.99298
Sc	1.28688	1.04502	0.94633	1.03243	0.93759	0.88082	1.03235	0.93872	0.88503	0.98601
Ti	1.28709	1.04601	0.94568	1.03310	0.93869	0.88181	1.03302	0.93982	0.88599	0.99313
V	1.28730	1.04668	0.94847	1.03453	0.94097	0.87832	1.03422	0.94134	0.88237	1.05011
Cr	1.28744	1.04729	0.94961	1.03408	0.94043	0.88409	1.03412	0.94162	0.88829	1.03573
Mn	1.28759	1.04785	0.95046	1.03530	0.94222	0.88119	1.03519	0.94294	0.88519	1.02826
Fe	1.28785	1.04836	0.95095	1.03526	0.94230	0.88497	1.03517	0.94333	0.88903	1.03849
Co	1.28799	1.04884	0.95177	1.03568	0.94300	0.88558	1.03560	0.94404	0.88964	1.03361
Ni	1.28813	1.04928	0.95672	1.03607	0.94366	0.88616	1.03600	0.94469	0.89019	1.04177
Cu	1.28817	1.04967	0.95326	1.03645	0.94430	0.88669	1.03637	0.94530	0.89070	1.03000
Zn	1.28823	1.05004	0.95394	1.03678	0.94486	0.88718	1.03671	0.94586	0.89118	1.04952
Ga	1.28844	1.05041	0.95456	1.03709	0.94538	0.88763	1.03703	0.94639	0.89161	1.05955
Ge	1.28845	1.05074	0.95459	1.03740	0.94591	0.88805	1.03733	0.94689	0.89202	1.06267
As	1.28856	1.05106	0.95506	1.03768	0.94638	0.88844	1.03761	0.94735	0.89240	1.06961
Se	1.28866	1.05137	0.95554	1.03804	0.94675	0.89024	1.03870	0.94774	0.89386	1.05322
Br	1.28874	1.05165	0.95599	1.03895	0.94790	0.88744	1.03891	0.94850	0.89165	1.03607
Kr	1.28880	1.05190	0.95638	1.03850	0.94764	0.89109	1.03841	0.94862	0.89460	1.04972

Table 2. Comparisons of the level energies (Ryd) of $1s^2\{2,3,4,5\}l$ ($l \in$ s, p, d, f and g), $1s2l^2$ and 1s2s2p configurations in O^{5+}, Ar^{15+}, Fe^{23+}, and Kr^{33+} ions.

		O^{5+}				Ar^{15+}				Fe^{23+}			Kr^{33+}		
ID		NIST	AS	ZFS90[a]	AK04[b]	NIST	AS	ZFS90[a]	MAK04[c]	NIST	AS	ZFS90[a]	NIST	AS	ZFS90[a]
01	$1s^2 2s\ ^2S_{1/2}$		0.000000		0.00000	0.0	0.00000		0.0000		0.00000			0.00000	
02	$1s^2 2p\ ^2P_{1/2}$	0.878234	0.885329	0.87823	0.88628	2.34219	2.34880	2.341892	2.3562	3.57201	3.57439	3.57134	5.23598	5.23290	5.23475
03	$1s^2 2p\ ^2P_{3/2}$	0.883086	0.890058	0.88308	0.89103	2.57527	2.57944	2.574956	2.5991	4.74549	4.73129	4.74474	10.00839	9.89070	10.00750
04	$1s^2 3s\ ^2S_{1/2}$	5.832472	5.826466	5.83200	5.82511	38.0548	38.05927	38.06429	38.0548	84.49724	84.51062	84.51543	169.48656	169.62291	169.63354
05	$1s^2 3p\ ^2P_{1/2}$	6.070070	6.065717	6.07057	6.06464	38.6966	38.70796	38.71255	38.7021	85.46045	85.50093	85.50765	170.91725	171.06624	171.09615
06	$1s^2 3p\ ^2P_{3/2}$	6.071497	6.067110	6.07219	6.06604	38.7658	38.77551	38.78531	38.7758	85.81493	85.83660	85.86779	172.32971	172.39343	172.54406
07	$1s^2 3d\ ^2D_{3/2}$	6.147642	6.140864	6.15083	6.13912	39.0129	39.02340	39.03374	39.0180	86.19675	86.23172	86.24998	172.87647	172.98296	173.10265
08	$1s^2 3d\ ^2D_{5/2}$	6.148107	6.141287	6.15127	6.13954	39.0347	39.04492	39.05505	39.0397	86.32068	86.34104	86.36023	173.32299	173.42539	173.55099
09	$1s^2 4s\ ^2S_{1/2}$	7.770338	7.763129	7.76875	7.76151	51.0833	51.08958	51.09489	51.0833	113.58397	113.60725	113.61331	227.97168	228.13298	228.17475
10	$1s^2 4p\ ^2P_{1/2}$	7.867276	7.860599	7.86576	7.85910	51.3477	51.35636	51.36169	51.3502	113.98948	114.01475	114.02490	228.56400	228.72479	228.77743
11	$1s^2 4p\ ^2P_{3/2}$	7.867859	7.861184	7.86650	7.85969	51.3766	51.38454	51.39182	51.3809	114.13529	114.15331	114.17190	229.15633	229.26209	229.38747
12	$1s^2 4d\ ^2D_{3/2}$	7.899593	7.892053	7.90104	7.89029	51.4777	51.48743	51.49693	51.4820	114.26560	114.31700	114.33359	229.39325	229.50560	229.62266
13	$1s^2 4d\ ^2D_{5/2}$	7.899788	7.892230	7.90104	7.89046	51.487	51.49647	51.50574	51.4911	114.32027	114.36279	114.38504	229.58462	229.68968	229.80641
14	$1s^2 4f\ ^2F_{5/2}$	7.901393	7.893360	7.90986	7.89157		51.50171	51.51750	51.4962	114.34214	114.37170	114.39974		229.70323	229.82846
15	$1s^2 4f\ ^2F_{7/2}$	7.901478	7.893450	7.90986	7.89166		51.50626	51.52265	51.5008	114.37860	114.39475	114.42179		229.79623	229.91665
16	$1s^2 5s\ ^2S_{1/2}$	8.645099	8.637644	8.64272	8.63594	57.041	57.05568	57.06005	57.0496	126.89804	126.96011	126.96791	254.82672	254.99054	255.04564
17	$1s^2 5p\ ^2P_{1/2}$	8.694217	8.686654	8.69123	8.68501	57.180	57.19053	57.19529	57.1847	127.06161	127.16606	127.17371	255.12744	255.28873	255.35433
18	$1s^2 5p\ ^2P_{3/2}$	8.694217	8.686952	8.69123	8.68531	57.195	57.20475	57.21072	57.2002	127.13633	127.23498	127.25455	255.56484	255.54925	255.66303
19	$1s^2 5d\ ^2D_{3/2}$	8.710355	8.702686	8.70887	8.70091	57.247	57.25702	57.26437	57.2515	127.21744	127.31804	127.33540	255.65597	255.67253	255.78062
20	$1s^2 5d\ ^2D_{5/2}$	8.710437	8.702777	8.70887	8.70100	57.251	57.26162	57.26878	57.2562	127.26118	127.34119	127.35745		255.76451	255.87617
21	$1s^2 5f\ ^2F_{5/2}$	8.711531	8.703418	8.71328	8.70163		57.26457	57.27467	57.2591		127.34619	127.36480		255.77203	255.89087
22	$1s^2 5f\ ^2F_{7/2}$	8.711531	8.703464	8.71328	8.70169		57.26689	57.27687	57.2614		127.35792	127.37950		255.81911	255.93497
23	$1s^2 5g\ ^2G_{7/2}$	8.711622	8.703473	8.71769	8.70168		57.26695	57.28128	57.2615		127.35800	127.37950		255.81914	255.94232
24	$1s^2 5g\ ^2G_{9/2}$	8.711622	8.703501	8.71769	8.70171		57.26834	57.28275	57.2629		127.36507	127.38685		255.84760	255.97172
25	$1s2s^2\ 2S_{1/2}$		40.585777			226.30	226.6709			485.12030	486.08392		950.487984	952.72430	
26	$1s2s2p\ 4P_{1/2}$	40.736371	40.855106			226.90	227.2355			486.09718	486.87277		951.964237	953.70746	
27	$1s2s2p\ 4P_{3/2}$		40.857635			226.96	227.3231			486.31589	487.23162		952.693251	954.68439	
28	$1s2s2p\ 4P_{5/2}$		40.861885			227.12	227.4864				488.07919			958.51599	
29	$1s2s2p\ 2P_{1/2}$	41.715072	41.492359				229.1038			489.02144	489.84686		956.329206	958.26788	
30	$1s2s2p\ 2P_{3/2}$		41.495632				229.2342			489.64383	490.58551		959.618880	961.74469	
31	$1s2p^2\ 4P_{1/2}$		41.831535			229.45	229.7814			490.30724	491.08856		958.880754	960.47711	
32	$1s2s2p\ 2P_{1/2}$		41.912865			229.61	230.0148			490.70911	491.60388		961.213598	963.19415	
33	$1s2p^2\ 4P_{3/2}$		41.834080			229.55	229.8833			490.91779	491.68264		962.133977	963.71863	
34	$1s2s2p\ 2P_{3/2}$		41.914692			229.67	230.0757			490.90867	491.82028		961.796809	963.83093	
35	$1s2p^2\ 4P_{5/2}$		41.838272			229.67	230.0271			491.33697	492.22747		962.972343	964.90558	
36	$1s2p^2\ 2D_{3/2}$	42.077756	42.250854			230.72	231.1017			492.63826	493.55090		964.612624	966.36713	
37	$1s2p^2\ 2P_{1/2}$		42.338909				231.3519			492.77677	493.70593		964.211666	966.11713	
38	$1s2p^2\ 2D_{5/2}$		42.251091			230.73	231.1496			493.10392	494.06726		967.756495	969.76538	
39	$1s2p^2\ 2P_{3/2}$		42.344051				231.5829			494.08444	495.01052		969.524353	971.48383	
40	$1s2p^2\ 2S_{1/2}$	42.719288	42.946438				232.8003			495.48870	496.47699		971.082620	973.03540	

Notes. AS denotes the present AUTOSTRUCTURE calculation. NIST refers to experimentally derived data in NIST compilation v3[2]. [(a)] Refers to the work of Zhang et al. (1990) using the Dirac-Fock-Slater method. [(b)] Refers to the work of Aggarwal & Keenan (2004a) using GRASP. [(c)] Refers to the work of McKeown et al. (2004b) using GRASP.

Table 3. Comparisons of line strengths S for K-shell transitions in ions (O^{5+}, Ar^{15+}, Fe^{23+} and Kr^{33+}) spanning sequence.

		O^{5+}		Ar^{15+}			Fe^{23+}				Kr^{33+}	
Label	$i-j$	present	GS83[a]	present	WBB02[b]	GS83[a]	present	WBB02[b]	MCDF[c]	BMK03[d]	present	GS83
v	1–26	2.45-7	2.74-7	7.82-6	7.64-6	8.06-6	2.52-5	2.46-5	3.16-5	3.23-5	4.36-5	4.73-5
u	1–27	1.24-6	1.39-6	4.45-5	4.36-5	4.63-5	1.73-4	1.69-4	2.00-4	2.01-4	3.54-4	3.85-4
	1–28	8.22-9		5.36-8		5.68-8	1.17-7			1.19-7	2.26-7	
r	1–29	2.64-2	2.81-2	5.13-3	5.24-3	5.09-3	1.85-3	1.88-3	1.85-3	1.92-3	6.15-4	6.22-4
q	1–30	5.32-2	5.70-2	1.19-2	1.21-2	1.24-2	5.87-3	5.86-3	5.64-3	5.99-3	2.66-3	2.94-3
t	1–32	3.10-3	3.38-3	1.22-3	1.12-3	1.45-3	1.17-3	1.13-3	1.06-3	1.18-3	8.72-4	1.01-3
s	1–34	5.79-3	5.96-3	7.72-4	6.15-4	6.99-4	6.29-5	3.34-5	4.08-5	5.29-5	4.64-5	3.08-5
p	2–25	6.59-4	5.15-4	1.24-4	1.24-4	1.11-4	6.20-5	6.17-5	5.52-5	6.20-5	3.54-5	3.37-5
i	2–31	4.89-7	5.15-7	2.10-5	2.07-5	2.17-5	1.14-4	1.12-4	1.28-4	1.41-4	2.93-4	3.18-4
g	2–33	7.63-9		4.28-7	4.23-7	5.43-7	1.37-6	1.34-6	4.42-7	5.82-7	2.20-6	2.49-6
k	2–36	2.48-2	2.71-2	7.13-3	7.10-3	7.27-3	3.88-3	3.86-3	3.78-3	4.01-3	2.01-3	2.22-3
d	2–37	2.98-2	3.17-2	6.76-3	6.77-3	7.03-3	3.32-3	3.31-3	3.17-3	3.39-3	1.46-3	1.60-3
b	2–39	1.36-2	1.48-2	1.27-3	1.30-3	1.47-3	1.50-4	1.55-4	9.58-5	1.23-4	1.30-5	1.53-5
n	2–40	4.07-3	4.50-3	5.23-4	5.21-4	4.89-4	6.22-5	6.10-5	6.77-5	6.46-5	1.47-6	9.32-7
o	3–25	1.30-3	1.01-3	1.97-4	1.98-4	1.73-4	6.35-5	6.34-5	5.64-5	6.42-5	1.56-5	1.47-5
	3–28			7.71-10			3.52-9			3.87-9	1.30-8	
h	3–31	1.49-8	5.22-8	7.71-7	8.08-7	1.25-6	1.11-6	1.16-6	8.29-7	5.95-7	6.93-8	2.40-7
f	3–33	1.53-6	1.31-6	3.76-5	3.67-5	3.59-5	9.93-5	9.75-5	1.26-4	1.38-4	1.36-4	1.45-4
e	3–35	3.18-6	3.28-6	1.30-4	1.27-4	1.31-4	5.88-4	5.75-4	6.17-4	6.96-4	9.42-4	1.02-3
l	3–36	3.49-3	4.39-3	3.54-6	1.53-6	3.84-6	3.89-4	3.79-4	4.89-4	4.68-4	4.52-4	4.74-4
c	3–37	1.47-2	1.55-2	2.73-3	2.72-3	2.70-3	1.00-3	9.90-4	9.83-4	1.03-3	4.26-4	4.51-4
j	3–38	4.23-2	4.72-2	9.29-3	9.26-3	9.70-3	3.95-3	3.94-3	3.81-3	3.95-3	1.35-3	1.50-3
a	3–39	7.54-2	7.95-2	1.69-2	1.69-2	1.74-2	7.64-3	7.61-3	7.19-3	7.74-3	3.49-3	3.85-3
m	3–40	8.55-3	9.71-3	2.37-3	2.39-3	2.58-3	1.47-3	1.48-3	1.40-3	1.52-3	8.33-4	9.30-4

Notes. Transition labels from Gabriel (1972). Note: $x \pm y \equiv x \times 10^{\pm y}$. Index numbers i, j are ID number in Fe^{23+}. [(a)] Refers to the work of Goett & Sampson (1983) using the Dirac-Fock-Slater method. [(b)] Refers to the work of Whiteford et al. (2002). [(c)] Refers to the work of Chen (1972) using the multiconfiguration Dirac-Fock method (MCDF). [(d)] Refers to the work of Bautista et al. (2003) using AUTOSTRUCTURE with relativistic two-body operators in single- and double-excited levels of the $n = 3$ complex and *term-energy-corrections*.

the transition energy. Bautista et al. (2003) took the relativistic two-body operator and *term-energy corrections* (TECs) into account in their AUTOSTRUCTURE calculation, resulting-in their line strengths being slightly larger than the present AS ones. Yet, they are still within 15% for most transitions (63%). For the highly-charged ion, Kr^{33+}, 73% of transitions agree to within 15% with the results of Goett & Sampson (1983).

Furthermore, a comparison of the line strength has been done here for outer-shell (dipole) transitions of ions spanning the sequence, see Fig. 1. For O^{5+}, the data of Zhang et al. (1990) is still the main source for astrophysical modelling and 66% of available transitions agree to within 5% of the present results. An excellent agreement is obtained between the present results and those of the GRASP calculation by Aggarwal & Keenan (2004a): 97% of available dipole transitions agree to within 5%. For Ar^{15+}, a comparison with the previous AS (Whiteford et al. 2002) and GRASP calculations (McKeown et al. 2004b) has been made: around 93% and 81%, respectively, of available transitions agree to within 5%. For Fe^{23+}, 98% of available outer-shell transitions from the ADAS database[4] (Whiteford et al. 2002) show agreement to within 5%. The present AS calculation also shows good agreement with the GRASP calculation performed by McKeown et al. (2004b) – 75% of available transitions show agreement to within 5%. For Kr^{33+}, somewhat worse agreement appears with the results of Zhang et al. (1990) which were obtained using Dirac-Slater atomic-structure approach. However, there are still about 57% of available transition showing agreement to within 10%.

Thus, we believe that the atomic structure of the ions spanning the sequence is reliable, and expect the uncertainty in collision strengths (Ωs) due to inaccuracies in the target structure to be correspondingly small.

3. Scattering

As demonstrated for inner-shell excitations of the Na-like iso-electronic sequence, including the astrophysically abundant Fe^{15+}, (Liang et al. 2008, 2009b) and the Li-like ions Ar^{15+} and Fe^{23+} (Ballance et al. 2001; Whiteford et al. 2002), the radiation- and Auger-damping effects significantly reduce the resonant enhancement of the collision strengths. In the Na-like iso-electronic sequence, the Auger damping effect was found to be the dominant damping mechanism over the entire sequence although the radiation damping increased quickly with increasing nuclear charge. The radiation- and Auger-damping effects have been incorporated into the present ICFT and Breit-Pauli R-matrix suite code via a complex optical potential as detailed by Gorczyca & Robicheaux (1999) and Robicheaux et al. (1995). For clarity, we give a brief description of the two damping effects for the specific case of Li-like ions. Over the sequence Be^{+}–Kr^{33+}, the four-electron resonance configurations are of the form $1s[2s, 2p][2s - 4f]nl$, and they can decay via the following channels:

$$1s[2s, 2p][2s - 4f]nl \rightarrow 1s^2[2s - 4f] + e^- \quad (3)$$

$$\rightarrow 1s^2 nl + e^- \quad (4)$$

$$\rightarrow 1s^2[2s, 2p][2s - 4f] + h\nu \quad (5)$$

$$\rightarrow 1s^2[2s - 4f]nl + h\nu. \quad (6)$$

[4] http://www.adas.ac.uk

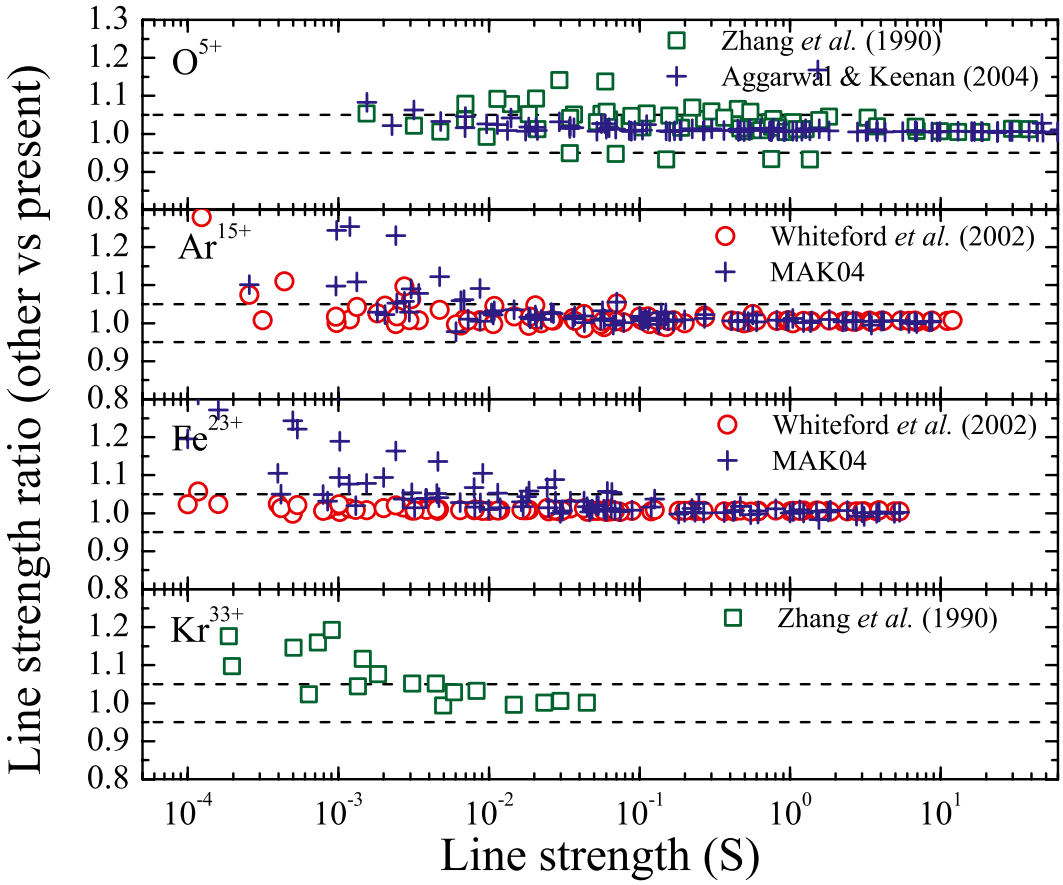

Fig. 1. Comparison of the line strength (S) of outer-shell dipole transitions for ions spanning the sequence. MAK04 corresponds to the GRASP calculation done by McKeown et al. (2004b). The horizontal dashed lines correspond to agreement within 5%. [Colour online]

The participator KL*n*/KM*n*/KN*n* Auger channel (Eq. (3)) scales as n^{-3} and is automatically described in the *R*-matrix method by the contribution to the close-coupling expansion from the right-hand side of Eq. (3). However, the spectator KLL/KLM/KLN Auger pathway (Eq. (4)) is independent of n and only low-n resonances ($n \leq 4$ here) are included explicitly in the close-coupling expansion. The higher-n are accounted-for by the complex optical potential which acts as a loss mechanism. The last two channels, Eqs. (5) and (6), represent radiation damping.

Our ICFT *R*-matrix calculations employed 40 (core-electron excitation) or 60 (valence-electron excitation) continuum basis orbitals per angular momentum to represent the $(N+1)$th-electron, over most of the sequence. For lower-charged ions, the number of continuum basis orbitals was increased. For example, the values were 46 and 65 in B^{2+} for the valence- and core-electron excitations, respectively. All partial waves from $J = 0$ to 41 were included explicitly and contributions from higher J-values were included using a "top-up" procedure (Burgess 1974; Badnell & Griffin 2001). The contributions from partial waves up to $J = 10$ were included in the exchange *R*-matrix, while those from $J = 11$ to 41 where included via a non-exchange *R*-matrix calculation. For the exchange calculation, a fine energy mesh (less than 0.005 Ryd, and even finer to 0.0002 Ryd for lower-charged ions) was used to resolve the majority of narrow resonances below the highest excitation threshold, which has been tested to be sufficient for the convergence of the effective collision strength. From just above the highest threshold excitation to a maximum energy of ten times the ionization potential for each ion, a coarse energy mesh ($1.0 \times 10^{-2} z^2$ Ryd, where $z = Z - 3$ is the residual charge of ion) was employed. For the non-exchange calculation, a step of $1.0 \times 10^{-2} z^2$ Ryd was used over the entire energy range.

We then used the infinite energy Born limits (non-dipole allowed) and line strengths (dipole allowed) from AUTOSTRUCTURE so that higher energy reduced collision strengths (Ω), as defined by Burgess & Tully (1992), can be found from interpolation in Burgess-Tully space for all additional higher energies. The effective collision strengths at 13 electron temperatures ranging from $2 \times 10^2 (z+1)^2$ K to $2 \times 10^6 (z+1)^2$ K are produced as the end product. The data were stored in the ADAS adf04 format (Summers 2004).

A separate Breit-Pauli DW calculation has been done for Fe^{23+} to study the importance of the effect of resonance enhancement. We find that it is still significant and widespread after Auger-plus-radiation damping has been taken into account. The DW approach has recently been incorporated into the AUTOSTRUCTURE code by Badnell (2011, see also AUTOSTRUCTURE code-log in APAP website[1]). It is self-consistent with the present *R*-matrix ICFT method in its calculation of the target structure.

4. Results and discussions

4.1. Comparisons with previous calculations for core-excitations

The present ICFT *R*-matrix results are compared with those of previous works for four ions (O^{5+}, Ar^{15+}, Fe^{23+} and Kr^{33+}) which span the range of calculated data for this iso-electronic sequence. Here we select a few inner-shell transition lines to test the accuracy of the present ICFT *R*-matrix calculations. An extensive comparison (all available excitation data from the ground level $1s^2 2s\ ^2S_{1/2}$) between the present ICFT *R*-matrix and previous calculations has been made for the four ions to check the broad accuracy and the resonant enhancement (when compared with

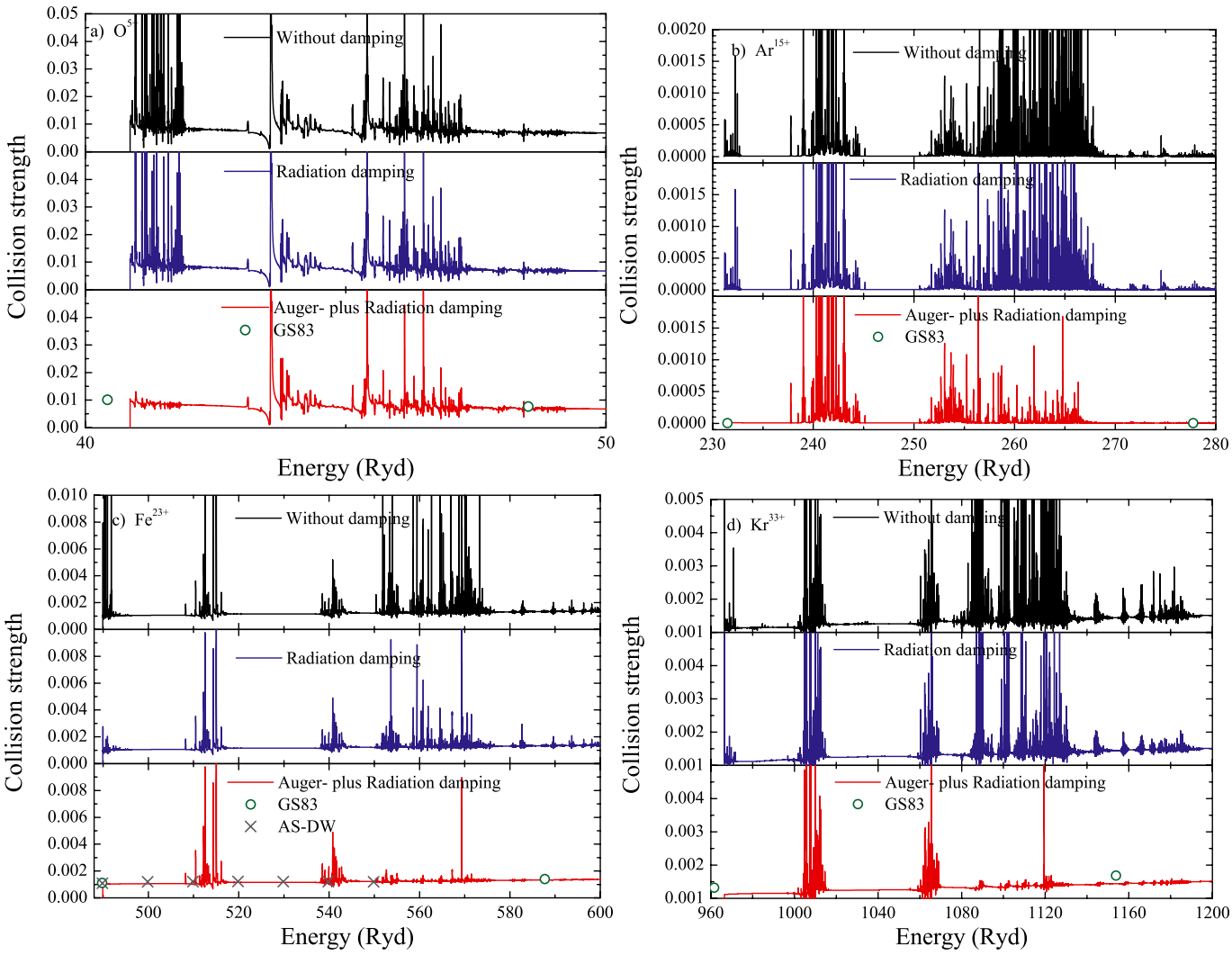

Fig. 2. Comparison of collision strengths Ω from the present ICFT *R*-matrix calculation in with those of Goett & Sampson (1983). **a)** O^{5+}: $1s^2 2s\ ^2S_{1/2} \rightarrow 1s2s2p\ ^4P_{3/2}$ excitation (u line in Table 3); **b)** Ar^{15+}: $1s^2 2s\ ^2S_{1/2} \rightarrow 1s2p^2\ ^2P_{1/2}$ excitation (1-37, ID is as list in Table 2); **c)** Fe^{23+}: $1s^2 2s\ ^2S_{1/2} \rightarrow 1s2s2p\ ^2P_{1/2}$ excitation (r line in Table 3). AS-DW corresponds to the present Breit-Pauli distorted-wave calculation using AUTOSTRUCTURE; **d)** Kr^{33+}: $1s^2 2p\ ^2P_{1/2} \rightarrow 1s2p^2\ ^2D_{3/2}$ excitation (k line in Table 3). [Colour online]

distorted-wave data) of the present ICFT *R*-matrix data. Earlier sequence calculations of core-electron impact excitation from the $1s^2\{2, 3\}l$ states were by Goett & Sampson (1983, hereafter GS83) and Sampson et al. (1985b) using the Coulomb-Born exchange method.

– O^{5+} To-date, there is no *R*-matrix calculation available for this ion. The background of the ordinary collision strength Ω of the present ICFT *R*-matrix calculation agrees well with that from the Coulomb-Born exchange method by Goett & Sampson (1983), as shown in Fig. 2 for the $1s2s2p\ ^4P_{3/2} \rightarrow 1s^2 2s\ ^2S_{1/2}$ transition line (the u line in Table 3). The resultant effective collision strengths (ϒ) are in agreement to within 10% over the entire temperature range, which is due to the scarce and weak resonances left after the Auger-plus-radiation damping has been taken into account. The undamped ϒ is higher than the results of Goett & Sampson (1983) by ∼20–35% for the temperature range $4 \times 10^2(z+1)^2$–$4 \times 10^3(z+1)^2$ K.
– Ar^{15+} A weak non-dipole transition line, due to $1s2p^2\ ^2P_{1/2} \rightarrow 1s^2 2s\ ^2S_{1/2}$, was selected for this ion. Figure 2b demonstrates that the background of the present calculation agrees well with the results of Goett & Sampson (1983). Strong resonances appear as expected for forbidden transitions, which significantly enhances the effective collision strengths over the temperature range $10^3(z+1)^2$–$10^5(z+1)^2$ K. We also find strong Auger and radiation damping effects on the Ω/ϒ for this transition, that will be discussed in detail later. At higher temperatures, the resonance contribution to the present *R*-matrix results becomes negligible, which leads-to good agreement with those of Goett & Sampson (1983). In a comparison with previous *R*-matrix data (Whiteford et al. 2002), our results with Auger-plus-radiation damping also show a good agreement over the entire temperature range, see Fig. 3b.
A complete dataset from Whiteford et al. (2002) is available from the OPEN-ADAS database[5]. Thus we have made an extensive comparison (all core-excitation data from the $1s^2 2l$ states) with them at the temperature (5.0×10^6 K) of peak Ar^{15+} fractional abundance in equilibrium (Bryans et al. 2009), as well as at a lower (5.0×10^5 K) and a higher (2.0×10^7 K) temperature. In this comparison, we adopt the configuration, total angular momentum, and energy ordering as the "good" quantum numbers to match

[5] http://open.adas.ac.uk

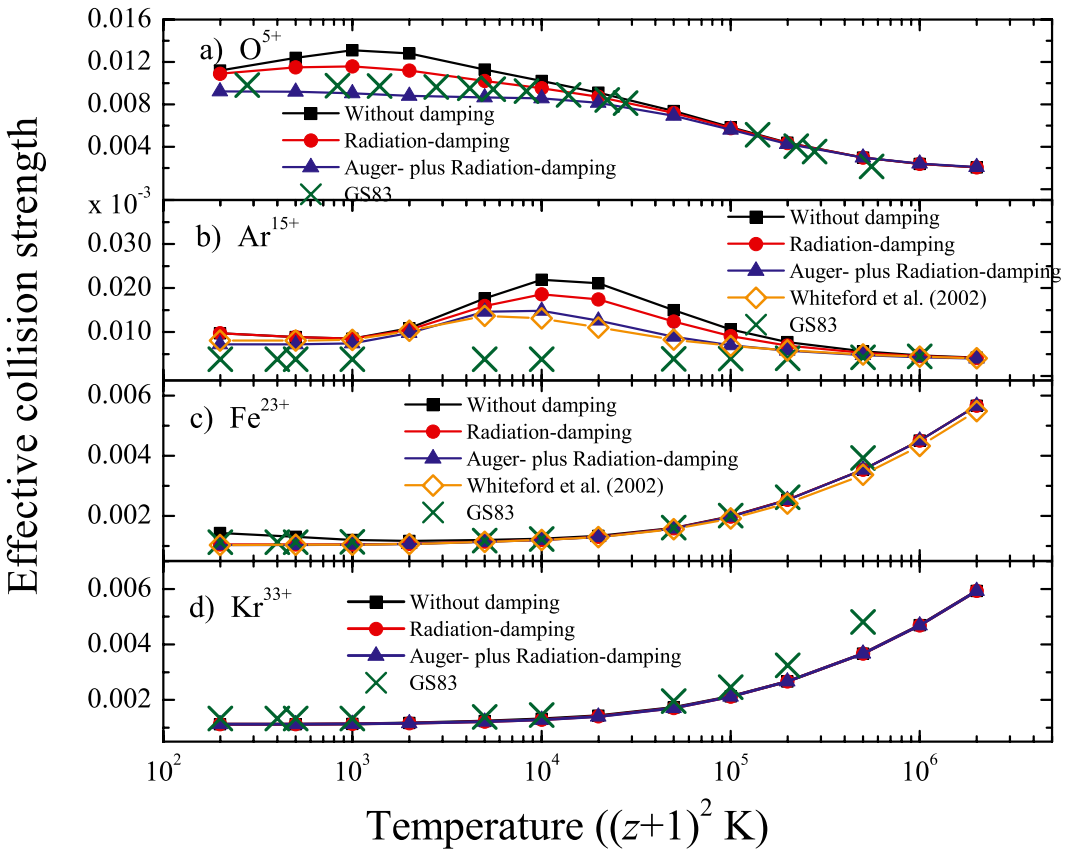

Fig. 3. Comparison of the effective collision strength ϒ between the present ICFT *R*-matrix calculation and previous results of Goett & Sampson (1983) and Whiteford et al. (2002). **a)** O^{5+}: $1s^2 2s\ ^2S_{1/2} \rightarrow 1s2s2p\ ^4P_{3/2}$; **b)** Ar^{15}: $1s^2 2s\ ^2S_{1/2} \rightarrow 1s2p^2\ ^2P_{1/2}$; **c)** Fe^{23+}: $1s^2 2s\ ^2S_{1/2} \rightarrow 1s2s2p\ ^2P_{1/2}$; **d)** Kr^{33+}: $1s^2 2p\ ^2P_{1/2} \rightarrow 1s2p^2\ ^2D_{3/2}$. [Colour online]

the transitions from the two different calculations. Recall, Whiteford et al. (2002) did not include any $n = 4$ states. We find that the ϒ results for 73% of core-excitations agree to within 20% at $T_e = 5.0 \times 10^6$ K. This slightly large difference between the two calculations with same method, is attributed to the different atomic models ($n = 3$ vs. $n = 4$). There are 88% of core-excitations to $n = 2$ levels showing agreement to within 20%, whereas the percentage is about 70% for core-excitations to $n = 3$ levels. This is consistent with the expectation that the influence of $n = 4$ states is stronger for the core-excitations to $n = 3$ than to $n = 2$. At the low and high temperatures, the percentage is 59% and 78%, respectively.

– Fe^{23+} A strong transition (the r line), due to $1s2s2p\ ^2P_{1/2} \rightarrow 1s^2 2s\ ^2S_{1/2}$, was selected for this ion. The ordinary collision strength Ω of Goett & Sampson (1983) shows a good agreement with the background of the present ICFT *R*-matrix calculation, as well as the present Breit-Pauli DW calculation using AUTOSTRUCTURE (AS-DW), see Fig. 2. For this ion, earlier *R*-matrix excitation data is available (Ballance et al. 2001; Whiteford et al. 2002). The present radiation damped calculation agrees well with the smaller-scale calculation by Ballance et al. (2001, see Fig. 7a in their work). Their corresponding Maxwellian-averaged ϒ is also in agreement with the present Auger-plus-radiation damping results and with those likewise of Whiteford et al. (2002). Due to the weak resonance contribution for this excitation, the calculation from the Coulomb-Born exchange method (GS83) also agrees well with the result of *R*-matrix calculation, see Fig. 3.
A complete dataset of Whiteford et al. (2002) is available from the OPEN-ADAS database[5]. Thus we make an extensive comparison as just done for Ar^{15+} at three temperatures (2.0×10^6 K, 2.0×10^7 K and 1.0×10^8 K). The percentage agreements are 68%, 78% and 81% at the low, middle (corresponding to peak abundance) and high temperatures, respectively.

– Kr^{33+} Another satellite line (the k line in Table 3) is selected to test the accuracy of the present calculation. Figure 2 displays that the background of the present ICFT *R*-matrix results is slightly lower than the Coulomb-Born exchange results of Goett & Sampson (1983) by ∼10%. This mirrors the reduction of the line strength demonstrated in Table 3. The resulting effective collision strengths agree with those from the Coulomb-Born exchange approach to within ∼10% over the entire temperature range, which is due to the scarcity of resonances for this satellite (k) line following damping. Auger-plus-radiation damping is significant for this line (see Fig. 2) and so the final damped resonance contribution is not significant for the effective collision strength at any temperature.

From the above comparison for the four specified ions (O^{5+}, Ar^{15+}, Fe^{23+} and Kr^{33+}) spanning the sequence, we believe that the present ICFT *R*-matrix results (Ω and ϒ) are reliable. For ions near neutral (below O^{5+}), *R*-matrix with pseudostates calculations are needed to consider ionization loss in the excitation, but the present are the best data to be made available to-date for these inner-shell transitions.

4.2. Comparisons with previous calculations for valence-excitations

As mentioned in the introduction, most available valence-excitation data is from the (relativistic) distorted-wave method (Zhang et al. 1990). We select one dipole transition line ($1s^2 4p\ ^2P_{1/2} \rightarrow 1s^2 2s\ ^2S_{1/2}$) and one non-dipole transition line ($1s^2 4d\ ^2D_{3/2} \rightarrow 1s^2 2s\ ^2S_{1/2}$) to test the accuracy of the present

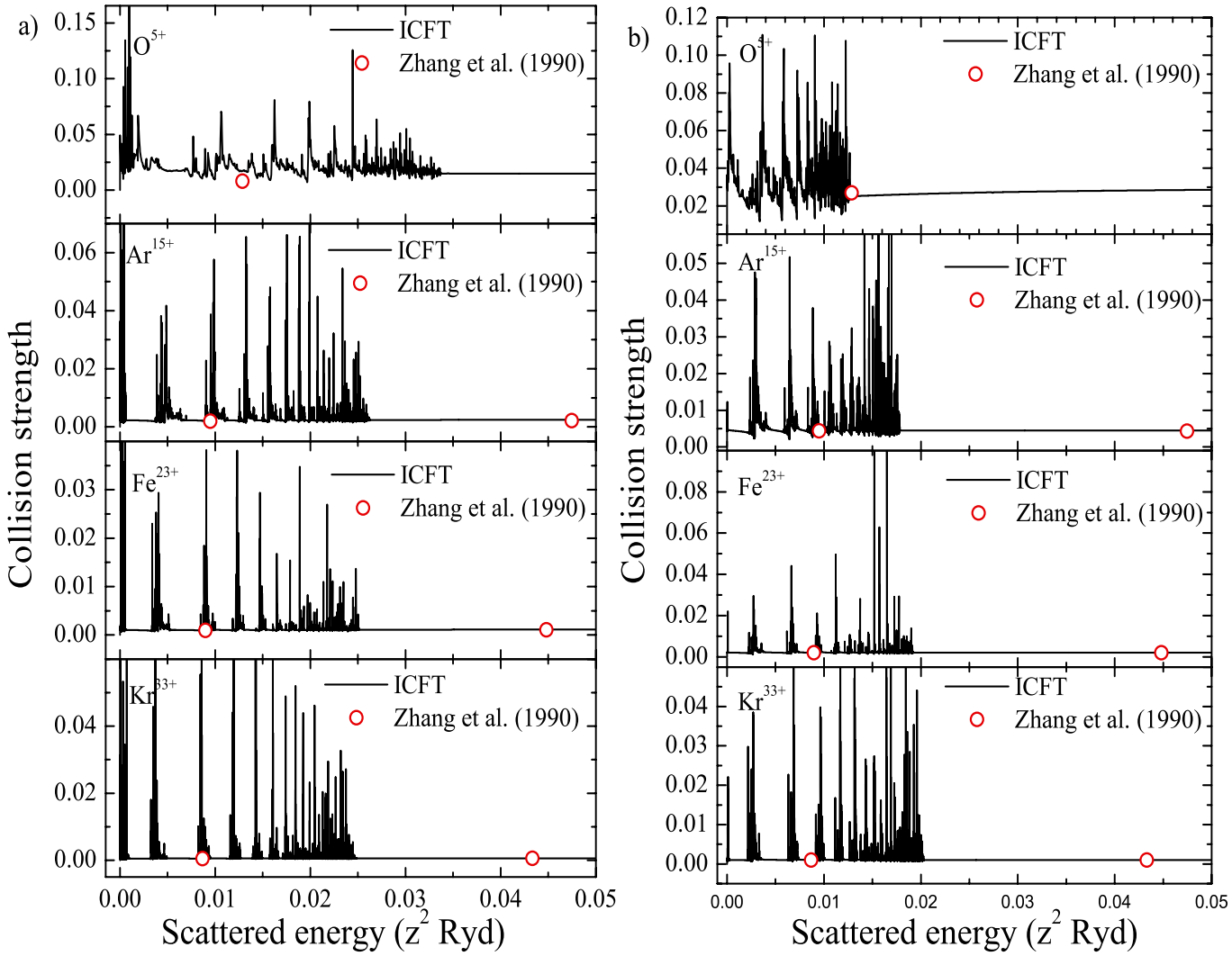

Fig. 4. Collision strengths Ω from the present ICFT *R*-matrix calculation and DW data (Zhang et al. 1990) for the dipole $1s^2 4p\ ^2P_{1/2} \rightarrow 1s^2 2s\ ^2S_{1/2}$ transition (*left*) and non-dipole $1s^2 4d\ ^2D_{3/2} \rightarrow 1s^2 2s\ ^2S_{1/2}$ transition (*right*) of ions (O^{5+}, Ar^{15+}, Fe^{23+} and Kr^{33+}) spanning the sequence. Note: The scattered electron energy is in unit of z^2 Ryd (z is the residual charge). [Colour online]

ICFT *R*-matrix calculations, see Fig. 4. The background of the collision strength Ω agrees well with the distorted-wave calculation for ions (O^{5+}, Ar^{15+}, Fe^{23+} and Kr^{33+}) spanning the sequence.

For the cosmic abundant ion Fe^{23+}, various *R*-matrix calculations including Breit-Pauli (Berrington & Tully 1997), ICFT (Whiteford et al. 2002) and DARC (McKeown 2005) are available. In the results of Whiteford et al. (2002), McKeown (2005, see Figs. 7.13–7.16) noticed that there are strong resonances, resonance shifts and background enhancement around thresholds for some outer-shell transitions when compared with her DARC calculation. The ordinary and effective collision strengths for $1s^2 4d\ ^2D_{3/2} \rightarrow 1s^2 4d\ ^2D_{5/2}$ are shown in Fig. 5 to illustrate this problem. A hard-copy comparison of Ω indicates that the present ICFT *R*-matrix calculation agrees well with the DARC calculation by McKeown (2005) – electronic results for McKeown (2005) are not available – which is confirmed by the effective collision strength ϒ, see the inset panel. The numerical problem in the work of Whiteford et al. (2002) has been traced to the treatment of the inner-region exchange integrals for high-L partial waves. The problem and solution is discussed in detail by Berrington (2006) and was incorporated into the Breit-Pauli *R*-matrix codes at the time (2006) – the ICFT method uses the standard inner-region Breit-Pauli codes. Moreover, an extensive comparison (see Table 4[6]) has been made for transitions with a large disagreement as reported by McKeown (2005) and they show good agreement between the present ICFT and DARC calculations. This demonstrates that the present results for outer-shell excitations are reliable for diagnostic modelling application.

A complete set of effective collision strengths for O^{5+} obtained using DARC (Aggarwal & Keenan 2004a) is available electronically. Comparison with the present results shows agreement to within 20% for 97% of all excitations at the temperature ($T_e = 3.2 \times 10^5$ K) of peak fractional abundance in equilibrium (Bryans et al. 2009). This provides further support that the present results are reliable over the sequence. For ions near neutral, viz. C^{3+}, Griffin et al. (2000) performed an LS-coupling *R*-matrix with 32 pseudostates (5s, 5p, 5d, 5f ⋯ 12s, 12p, 12d and 12f) calculation to determine ionization loss in the valence-excitations, and found the reduction of the effective collision strengths to be less than 10% for excitations up to $n = 3$. For excitations to the $n = 4$ shell, the pseudostate results are typically

[6] Different energy meshes are used around threshold in the two calculations, present: $10^{-5} z^2$ Ryd ($z = 23$ in Fe^{23+}); DARC: 5.0×10^{-4} Ryd.

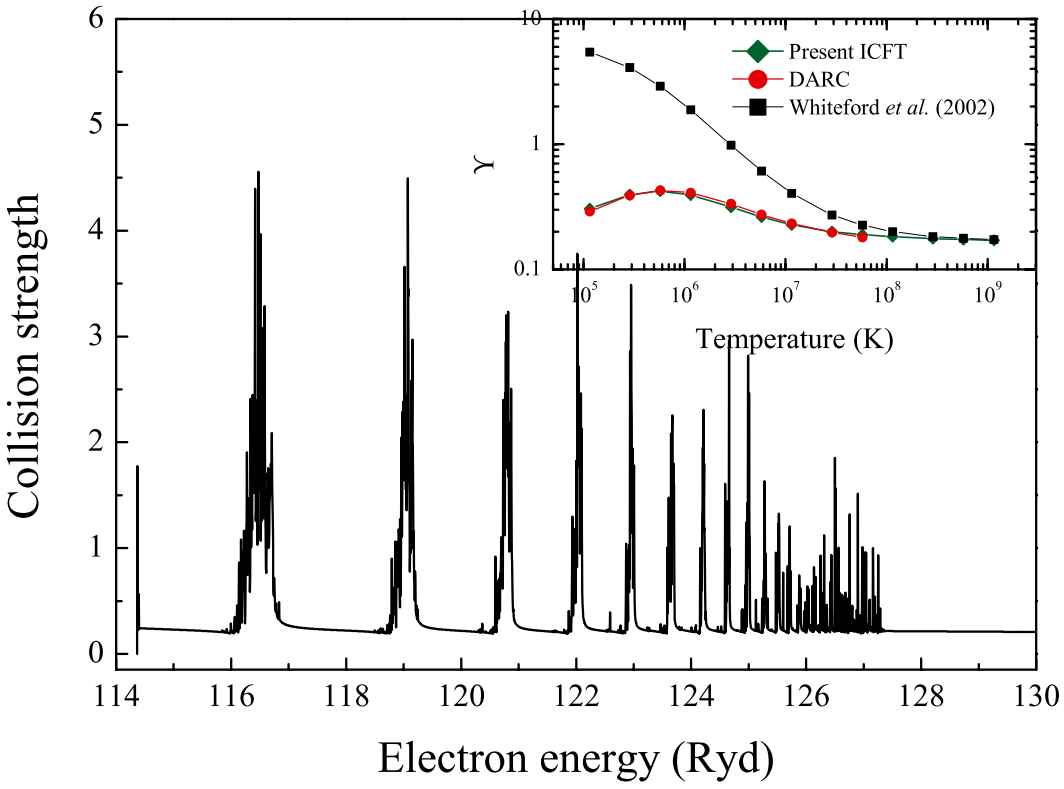

Fig. 5. Collision strength Ω for the $1s^2 4d\ ^2D_{3/2} \rightarrow 1s^2 4d\ ^2D_{5/2}$ excitation, as well as the comparison of resultant effective collision strength ϒ with previous works of McKeown (2005) using DARC *R*-matrix suite code and Whiteford et al. (2002). [Colour online]

Table 4. Comparisons of effective collision strength ϒ for Fe^{23+} from the DARC calculation of McKeown (2005), the present ICFT and the previous ICFT by Whiteford et al. (2002, WBB02).

Transitions	1.15×10^5 K			1.15×10^7 K			5.76×10^7 K		
	DARC	ICFT	WBB02	DARC	ICFT	WBB02	DARC	ICFT	WBB02
$2p\ ^2P_{1/2}-4p\ ^2P_{3/2}$	2.41-3	3.39-3	7.09-3	1.24-3	1.28-3	1.31-3	8.21-4	8.19-4	8.38-4
$2p\ ^2P_{3/2}-4p\ ^2P_{1/2}$	3.40-3	5.22-3	1.13-2	1.29-3	1.26-3	1.33-3	8.56-4	8.12-4	8.48-4
$3d\ ^2D_{3/2}-3d\ ^2D_{5/2}$	1.05-1	1.05-1	1.05+1	1.34-1	1.32-1	4.62-1	6.56-2	6.45-2	1.32-1
$3d\ ^2D_{3/2}-4d\ ^2D_{3/2}$	1.43-1	1.35-1	4.77-1	1.42-1	1.40-1	1.53-1	1.44-1	1.41-1	1.41-1
$3d\ ^2D_{3/2}-4d\ ^2D_{5/2}$	2.90-2	2.85-2	1.61-1	1.62-2	1.62-2	2.00-2	1.01-2	1.04-2	1.11-2
$3d\ ^2D_{3/2}-4f\ ^2F_{7/2}$	4.94-2	4.90-2	1.24-1	2.65-2	2.58-2	2.76-2	1.52-2	1.50-2	1.54-2
$3d\ ^2D_{3/2}-5d\ ^2D_{3/2}$	2.82-2	2.58-2	7.83-2	2.54-2	2.44-2	2.65-2	2.57-2	2.45-2	2.52-2
$3d\ ^2D_{3/2}-5d\ ^2D_{5/2}$	9.22-3	8.65-3	2.31-2	4.13-3	4.07-3	4.49-3	2.57-3	2.56-3	2.65-3
$3d\ ^2D_{5/2}-4p\ ^2P_{1/2}$	2.78-2	3.46-2	8.18-2	5.88-3	5.53-3	6.13-3	3.36-3	3.25-3	3.36-3
$3d\ ^2D_{5/2}-4d\ ^2D_{3/2}$	3.02-2	2.95-2	1.78-1	1.63-2	1.63-2	2.01-2	1.03-2	1.06-2	1.12-2
$3d\ ^2D_{5/2}-4d\ ^2D_{5/2}$	2.20-1	2.18-1	1.29+0	2.21-1	2.19-1	2.63-1	2.21-1	2.18-1	2.26-1
$4p\ ^2P_{1/2}-4d\ ^2D_{5/2}$	7.74-2	7.86-2	1.98-1	7.75-2	7.78-2	7.99-2	7.45-2	7.67-2	7.76-2
$4p\ ^2P_{1/2}-4f\ ^2F_{7/2}$	6.10-2	6.00-2	1.91-1	3.99-2	3.72-2	3.76-2	2.34-2	2.30-2	2.29-2

Notes. $x \pm y \equiv x \times 10^{\pm y}$.

20% smaller, with one transition (2s – 4d) being 30%. However, the present are the best *J*-resolved data to be made available to-date.

Finally, we note that dipole transitions between closely-spaced levels, e.g. $5f_j-5g_{j'}$, are dominated by contributions from high angular momentum and these come mainly from the Coulomb-Bethe "top-up". The top-up is inversely proportional to the energy separation. Our sequence work makes use of calculated energies. This can give rise to large errors in the top-up. This has no practical consequences. The excitation rates are very large and so, along with proton collisions, establish statistical values for these level populations independently of the precise value of the excitation rate.

4.3. Damping effects along the sequence

As shown in Fig. 2, radiation damping significantly reduces the resonance strength of inner-shell transitions. The inclusion of Auger damping further reduces the resonance strength. Correspondingly, the resonance enhancement of the effective collision strengths is reduced, see Fig. 3. For some strong excitations, the resonance contribution to the ϒ decreases to the level of 10%, e.g. the $1s^2 2s\ ^2S_{1/2} \rightarrow 1s2s2p\ ^2P_{1/2}$ excitation line of Fe^{23+} shown in Fig. 3. However, for some weak transition lines, the damped resonance contribution to the effective collision strength is still non-negligible and leads to significantly higher results than those without resonances (see Fig. 3 for Ar^{15+}), e.g. the work of Goett & Sampson (1983) using the Coulomb-Born exchange method.

In the inner-shell excitations for the Na-like iso-electronic sequence, Liang et al. (2009b) clearly demonstrated that radiation damping increases steadily with increasing of nuclear charge Z, but the Auger damping effect still plays an important role on the reduction of the resonance enhancement of Υ over the iso-electronic sequence.

Here we illustrate the radiation and Auger-plus-radiation damping effects along the sequence by a scatter plot of the ratios of damped to undamped (or only radiation damped) Υ at $T_e = 10^4(z+1)^2$ K for dipole transitions of O^{5+} (Fig. 6a), Ar^{15+} (Fig. 6c), Fe^{23+} (Fig. 6e) and Kr^{33+} (Fig. 6g). The widespread effect of the radiation and Auger-plus-radiation damping effects is illustrated. For the low-charge ion (O^{5+}) the radiation damping is small, being less than 10% for 99% of all dipole core-excitations at the temperature of $10^4(z+1)^2$ K. The Auger damping is the prominent factor for the reduction of resonance enhancement of Υ. It can up to a factor of 5 for a few dipole transitions. For Ar^{15+}, the radiation damping is less than 10% for most (94%) of the dipole transitions. The Auger damping is stronger and larger than a factor of 2 for 30% of the illustrated dipole transitions. For Fe^{23+}, the radiation damping increases, but the Auger damping is still the dominant and stronger damping effect in the reduction of resonance enhancement of Υ. About 30% of dipole transitions show an Auger damping reduction of over a factor of 2 when compared with the radiation damped Υ. For higher-charge ions, e.g. Kr^{33+}, the radiation damping is greater than 30% for 10% of the dipole transitions. But, Fig. 6g demonstrates that Auger damping is still the dominant resonance damping reduction of Υs at $T_e = 10^4(z+1)^2$ K. Additionally, we notice that there are a few weak transitions with the Υ_R/Υ_U ratio being slightly larger than unity. This was found to be due to the low resolution of the undamped resonances. Recall, damping both broadens and reduces the height of resonance profiles.

An illustrative way to quantify the information in the scatter plot is to count how many transitions differ by more than a given value. In Figs. 6b, d, f and h, we show the percentage of the dipole transitions where the Auger-plus-radiation damping effect, or radiation or Auger damping effects alone, are at least 10%, 20% and 30% for the four ions. Here, 0%, <1%, 3% and 10% of dipole transitions show a radiation damping effect of more than 30% at $T_e = 10^4(z+1)^2$ K for O^{5+}, Ar^{15+}, Fe^{23+} and Kr^{33+}, respectively. The percentage for higher-charge ions, e.g. Fe^{23+} and Kr^{33+}, is higher than that of lower-charge ions. This illustrates that the radiation damping is more widespread for higher-charge ions, as one would expect. There are about 36%, 43%, 41% and 37% of dipole transitions showing a further Auger damping of more than 30% at the temperature of $10^4(z+1)^2$ for O^{5+}, Ar^{15+}, Fe^{23+} and Kr^{33+}, respectively. This means that the Auger damping is still the dominant damping effect over the entire sequence.

4.4. Resonant enhancement for core-excitations

The Auger-plus-radiation damping effect significantly reduces the resonance enhancement of the effective collision strength for core-excitations. Does this mean that one can use non-resonant excitation data such as DW? Here we investigate it statistically by comparing distorted-wave (AS-DW) and R-matrix (ICFT) calculations for Fe^{23+}. The exact same atomic structure was used for the AS-DW calculation as has been described and used in the R-matrix calculation. This eliminates differences in the collision data due to the use of different atomic structures. The scatter plot in Fig. 7 demonstrates that the resonant enhancement can be larger than a factor of 2 for some core-excitations. The percentage is about 66% and 59% of all core-excitations at $T_e = 2.0 \times 10^5$ and 2.0×10^7 K, respectively. So a complete sequence calculation with resonances is still necessary. The non-resonant DW results could be supplemented by resonances calculated perturbatively. This is just the complement of dielectronic recombination. It is beyond the scope of the present work.

4.5. Iso-electronic trends

As noted in the previous sequence works (Witthoeft et al. 2007; Liang et al. 2009b, 2010), the level mixing effect for higher excited levels strongly affects the behaviour of the Υ along the sequence. Here, we also take configuration, total angular momentum J and energy ordering for level matching in the comparison between different calculations and the investigation of Υ along the iso-electronic sequence. This satisfactorily eliminates uncertainty originating from the non-continuity of level-ordering along the sequence. The choice of reference ion, Fe here, is irrelevant of course.

In Fig. 8, we show the effective collision strength Υ at $T_e/(z+1)^2 = 5 \times 10^2$, 10^3 and 10^4 K along the sequence for a few satellite lines in Li-like ions: at the low temperature of $5 \times 10^2(z+1)^2$ K, spikes and/or dips are observed at low charges for some transitions, e.g. $1s^2 2p\ ^2P_{3/2} \rightarrow 1s2s2p\ ^4P_{1/2}$ (3–26). With increasing temperature, the spikes and/or dips disappear, as expected, because the resonance contribution becomes weaker and eventually negligible. For K-shell excitations, the behaviour of Υ along the sequence differs from the L-shell, for example F-like (Witthoeft et al. 2007) and Ne-like sequences (Liang & Badnell 2010). The irregularity appears only for the low-charged ions. Above $Z \sim 14$, the effective collision strengths show a smooth behaviour. This is due to the high core-excitation energy. KMn resonances are all positioned well above threshold while KLn can only Auger to the final-state for high-n at high-charge and so there is little variation. Only at low-charge do low-n KLn resonances come into play. The "precise" n-value can be estimated from the Rydberg formula: $n \approx z/\sqrt{E_{fj}}$, where f is the final state and j is an intermediate parent resonant state to which the Rydberg series of resonances converges. For example, for O^{5+} ($z = 5$) from Table 2 we have $E_{fj} = 2.36$ Ryd for the $40 \rightarrow 25$ ($j \rightarrow f$) core-Auger, giving $n = 4$ as the lowest KLn resonance for any excitation transition $i - 25$. The variation in n and energy spacing is relatively largest for the smallest n-values. This variation can then be seen in the Maxwell-averaged results.

5. Summary

We have performed 195-level (24-level) ICFT R-matrix calculations the of core- (valence-) electron-impact excitation of all ions of the Li-like iso-electronic sequence from Be^+ to Kr^{33+}.

Good agreement with the available experimentally derived data and the results of others for level energies and line strengths S for several specific ions (O^{5+}, Ar^{15+}, Fe^{23+}, and Kr^{33+}) spanning the iso-electronic sequence supports the reliability of the present R-matrix excitation data. This was confirmed specifically by detailed comparisons (including previously available R-matrix calculations) of Ω and Υ for O^{5+}, Ar^{15+}, Fe^{23+} and Kr^{33+}.

A problem for some Fe^{23+} outer-shell excitation transitions in the earlier ICFT calculation by Whiteford et al. (2002) was checked-for in the present calculations by comparison with the fully relativistic DARC calculation by McKeown (2005) and not found. It had been solved by a previous correction

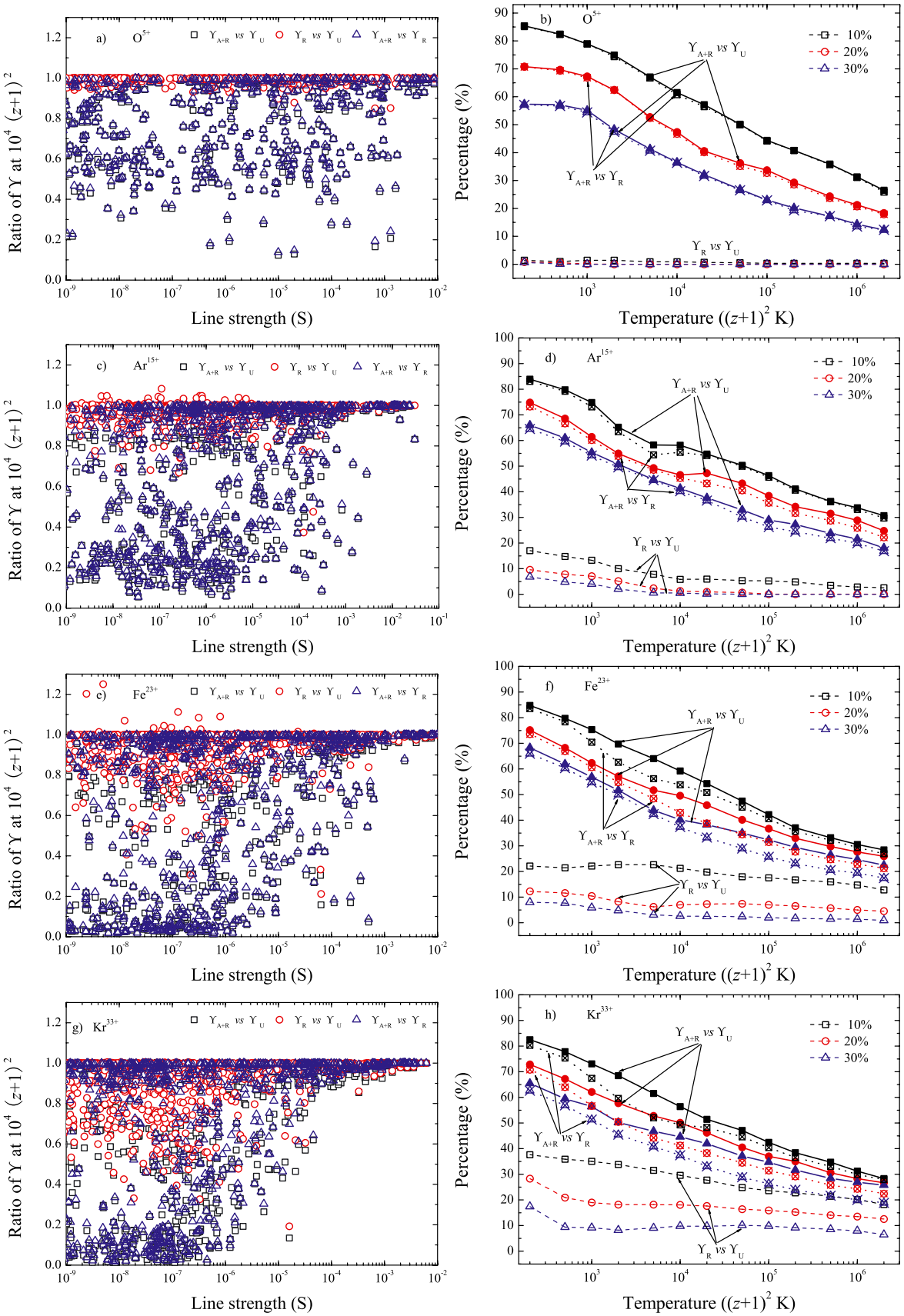

Fig. 6. *Left-hand panels*: scatter plots showing the ratio of the effective collision strength Υ with Auger-plus-radiation damping (Υ_{A+R}) or radiation damping (Υ_R) to without damping (Υ_U) or with radiation damping alone, as a function of line strength for dipole core-excitation of O^{5+} **a)**, Ar^{15+} **c)**, Fe^{23+} **e)** and Kr^{33+} **g)** at temperature of $10^4(z+1)^2$ K, where z is the ionic charge. *Right-hand panels*: percentage of the corresponding transitions where the effect of damping exceeds 10%, 20% and 30%. [Colour online]

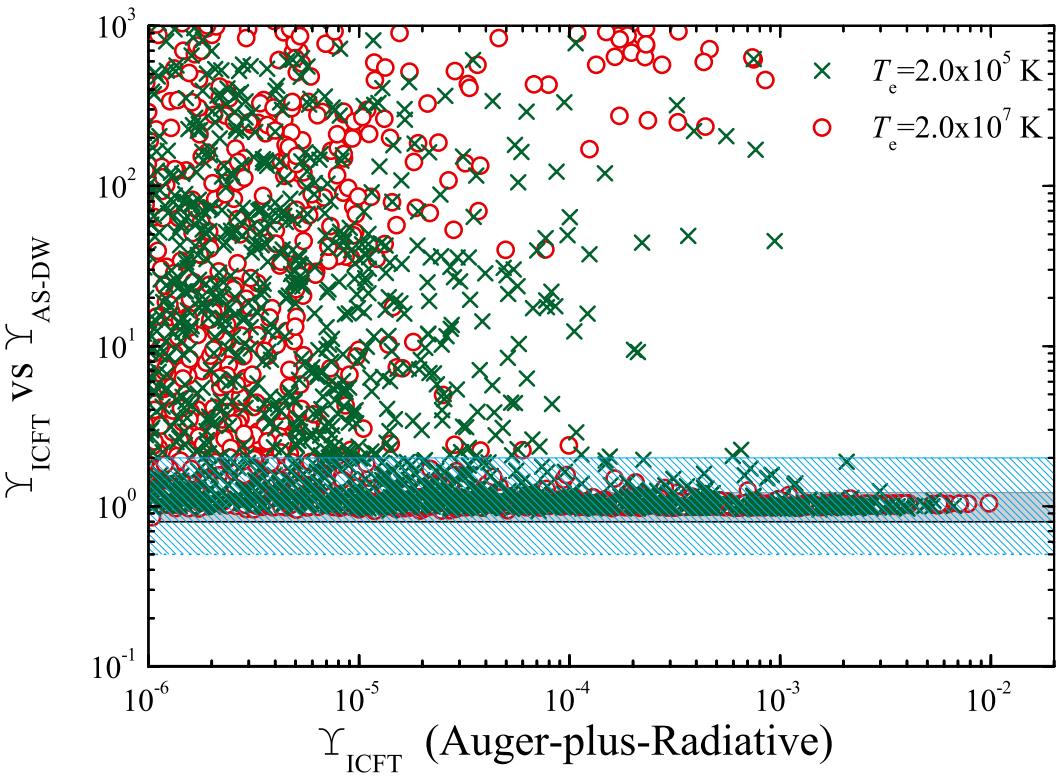

Fig. 7. The ratio of the effective collision strengths Υ for all core-excitations in Fe^{23+} between the present ICFT *R*-matrix and Breit-Pauli DW (AUTOSTRUCTURE) calculations at the temperature of 2.0×10^5 and 2.0×10^7 K. The filled and dashed regions correspond to a agreement of 20% and a factor 2, respectively. [Colour online]

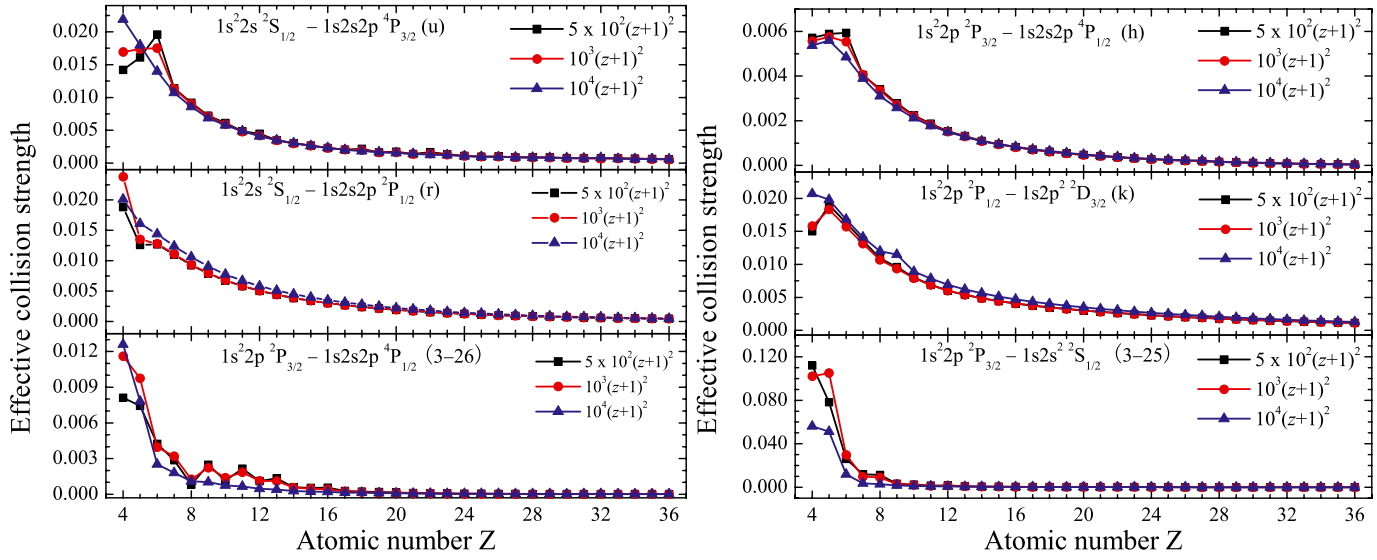

Fig. 8. Effective collision strengths Υ at temperatures of $T_e = 5\times10^2(z+1)^2$, 10^3, 10^4 K (here, $z = Z-3$) along the iso-electronic sequence. *Left-hand panels*: 1s2s2p $^4P_{3/2} \rightarrow 1s^2 2s\ ^2S_{1/2}$ (u line), 1s2s2p $^2P_{1/2} \rightarrow 1s^2 2s\ ^2S_{1/2}$ (r line) and 1s2s2p $^4P_{1/2} \rightarrow 1s^2 2p\ ^2P_{3/2}$ (3-26) transitions. *Right-hand panels*: 1s2p^2 $^4P_{1/2} \rightarrow 1s^2 2p\ ^2P_{3/2}$ (h line), 1s2p^2 $^2D_{3/2} \rightarrow 1s^2 2p\ ^2P_{1/2}$ (k line) and 1s2s^2 $^2S_{1/2} \rightarrow 1s^2 2p\ ^2P_{3/2}$ (3-25) transitions. [Colour online]

(Berrington 2006) to the inner-region Breit-Pauli codes which the ICFT method makes use of.

The present *R*-matrix excitation data is expected to be an important improvement on the current data (from Coulomb-Born exchange approximation) extensively used by the spectroscopic diagnostic modelling communities in astrophysics and magnetic fusion.

The Auger-plus-radiation damping effect along the sequence was examined, it is significant and widespread over the entire sequence and more-so for the higher-charge ions. For some inner-shell transitions (39% of available DW data to $1s^2 2l$ levels in Ar^{15+}), the damped effective collision strengths are still larger than those without the inclusion of resonances (by 20%). The Auger damping effect was found to be dominant in the reduction of resonance enhancement on the electron-impact excitation over the entire sequence, whereas the radiation damping is small for lower-charge ions but increases with increasing nuclear charge.

By excluding the level crossing effects on the Υ, we examined the iso-electronic trends of the effective collision strengths. A complicated pattern of spikes and dips of Υ at low temperatures was noted again along the sequence for some transitions with strong resonances, which precludes the generality of interpolation in *Z*. With increasing temperature, the resonance

effects decrease as expected. Such irregular effects are only seen at low-charges for inner-shell transitions since low-n resonances cannot straddle thresholds in high-charge ions.

The data are made available in the ADAS *adf04* format (Summers 2004) at the archives of the APAP[1], OPEN-ADAS[5] and and will be included in CHIANTI[7] database.

In conclusion, we have generated an extensive set of reliable excitation data, utilizing the ICFT *R*-matrix method, for spectroscopy/diagnostic research within the astrophysical and fusion communities. This will replace data from DW and Coulomb-Born exchange approaches presently used by these communities and its use can be expected to identify new lines and may overcome some shortcomings in present astrophysical modelling, as we have seen for Mg^{8+} (Del Zanna et al. 2008), Fe^{6+}, Fe^{7+} and Fe^{10+} (Del Zanna 2009a,b, 2010), Si^{9+} (Liang et al. 2009c) and Fe^{7+}–Fe^{15+} (Liang & Zhao 2010).

Acknowledgements. The work of the UK APAP Network is funded by the UK STFC under grant no. PP/E001254/1 with the University of Strathclyde.

References

Aggarwal, K. M., & Keenan, F. P. 2004a, Phys. Scr., 70, 222
Aggarwal, K. M., Keenan, F. P., & Heeter, R. F. 2010, Phys. Scr., 81, 015303
Badnell, N. R. 1986, J. Phys. B At. Mol. Opt. Phys., 19, 3827
Badnell, N. R. 2011, Comp. Phys. Comm., accepted
Badnell, N. R., & Griffin, D. C. 2001, J. Phys. B At. Mol. Opt. Phys., 34, 681
Ballance, C. P., Badnell, N. R., & Berrington, K. A. 2001, J. Phys. B At. Mol. Opt. Phys., 34, 3287
Ballance, C. P., Griffin, D. C., Colgan, J., Loch, S. D., & Pindzola, M. S. 2003, Phys. Rev. A, 68, 062705
Bautista, M. A., & Badnell, N. R. 2007, A&A, 466, 755
Bautista, M. A., Mendoza, C., Kallman, T. R., & Palmeri, P. 2003, A&A, 403, 339
Berrington, K. A. 2006, J. Phys. B At. Mol. Opt. Phys., 39, 3837
Berrington, K. A., & Tully, J. A. 1997, A&AS, 126, 105
Bryans, P., Landi, E., & Savin, D. W. 2009, ApJS, 167, 343
Burgess, A. 1974, J. Phys. B At. Mol. Opt. Phys., 7, L364
Burgess, A., & Tully, J. A. 1991, A&A, 254, 436
Chen, M. H. 1986, Atom. Data Nucl. Data Tables, 34, 301
Del Zanna, G. 2009a, A&A, 508, 501
Del Zanna, G. 2009b, A&A, 508, 513
Del Zanna, G. 2010, A&A, 514, A41
Del Zanna, G., Rozum, I., & Badnell, N. R. 2008, A&A, 487, 1203
Dere, K. P., Landi, E., Young, P. R., et al. 2009, A&A, 498, 915
Gabriel, A. H. 1972, MNRAS, 160, 99
Goett, S. J., & Sampson, D. H. 1983, Atom. Data Nucl. Data Tables, 29, 535
Gorczyca, T. W., & Badnell, N. R. 1996, J. Phys. B At. Mol. Opt. Phys., 29, L283
Gorczyca, T. W., & Robicheaux, F. 1999, Phys. Rev. A, 60, 1216
Griffin, D. C., Badnell, N. R., & Pindzola, M. S. 1998, J. Phys. B At. Mol. Opt. Phys., 31, 3713
Griffin, D. C., Badnell, N. R., & Pindzola, M. S. 2000, J. Phys. B At. Mol. Opt. Phys., 33, 1013
Liang, G. Y., & Badnell, N. R. 2010, A&A, 518, A64
Liang, G. Y., & Zhao, G. 2010, MNRAS, 405, 1987
Liang, G. Y., Whiteford, A. D., & Badnell, N. R. 2008, J. Phys. B At. Mol. Opt. Phys., 41, 235203
Liang, G. Y., Whiteford, A. D., & Badnell, N. R. 2009a, A&A, 500, 1263
Liang, G. Y., Whiteford, A. D., & Badnell, N. R. 2009b, J. Phys. B At. Mol. Opt. Phys., 42, 225002
Liang, G. Y., Whiteford, A. D., & Badnell, N. R. 2009c, A&A, 499, 943
McKeown, K. 2005, Ph.D. Thesis, Queen's University, Belfast
McKeown, K., Aggarwal, K. M., Keenan, F. P., & Rose, S. J. 2004b, Phys. Scr., 70, 295
Nahar, S. N., Oelgoetz, J., & Pradhan, A. K. 2009, Phys. Scr., 79, 055301
Oelgoetz, J., Fontes, C. J., Zhang, H. L., Nahar, S. N., & Pradhan, A. K. 2009, MNRAS, 394, 742
Phillips, K. J. H., Dubau, J., Sylwester, J., & Sylwester, B. 2006, ApJ, 638, 1154
Robicheaux, F., Gorczyca, T. W., Pindzola, M. S., & Badnell, N. R. 1995, Phys. Rev. A, 51, 1319
Sampson, D. H., Goett, S. J., Petrou, G. V., Zhang, H. L., & Clark, R. E. H. 1985a, Atom. Data Nucl. Data Tables, 32, 343
Sampson, D. H., Petrou, G. V., Goett, S. J., & Clark, R. E. H. 1985b, Atom. Data Nucl. Data Tables, 32, 403
Summers, H. P. 2004, The ADAS User manual version 2.6, http://www.adas.ac.uk/
Zhang, H. L., Sampson, D. H., & Clark, R. E. H. 1986, Atom. Data Nucl. Data Tables, 35, 267
Zhang, H. L., Sampson, D. H., & Fontes, C. J. 1990, Atom. Data Nucl. Data Tables, 44, 31
Whiteford, A. D., Badnell, N. R., Ballance, C. P., et al. 2002, J. Phys. B At. Mol. Opt. Phys., 3, 3729
Widing, K. G., & Purcell, J. D. 1976, ApJ, 204, L151
Witthoeft, M. C., Whiteford, A. D., & Badnell, N. R. 2007, J. Phys. B At. Mol. Opt. Phys., 40, 2969

[7] http://www.chianti.rl.ac.uk/